

Mechanistic insight into gold nanorod transformation in nanoscale confinement of ZIF-8

Cheongwon Bae¹, Jaedeok Lee¹, Lehan Yao², Suhyeon Park¹, Yeonju Lee¹, Jieun Lee¹, Qian Chen^{2,3,4,5}, and Juyeong Kim¹ (✉)

¹ Department of Chemistry and Research Institute of Natural Sciences, Gyeongsang National University, Jinju 52828, South Korea

² Department of Materials Science and Engineering, University of Illinois at Urbana-Champaign, Urbana, IL 61801, USA

³ Materials Research Laboratory, University of Illinois at Urbana-Champaign, Urbana, IL 61801, USA

⁴ Beckman Institute for Advanced Science and Technology, University of Illinois at Urbana-Champaign, Urbana, IL 61801, USA

⁵ Department of Chemistry, University of Illinois at Urbana-Champaign, Urbana, IL 61801, USA

© Tsinghua University Press and Springer-Verlag GmbH Germany, part of Springer Nature 2020

Received: 17 May 2020 / Revised: 5 August 2020 / Accepted: 7 August 2020

ABSTRACT

Core-shell hybrid nanomaterials have shown new properties and functions that are not attainable by their single counterparts. Nanoscale confinement effect by porous inorganic shells in the hybrid nanostructures plays an important role for chemical transformation of the core nanoparticles. However, metal-organic frameworks (MOFs) have been rarely applied for understanding mechanical insight into such nanoscale phenomena in confinement, although MOFs would provide a variety of properties for the confining environment than other inorganic shells such as silica and zeolite. Here, we examine chemical transformation of a gold nanorod core enclosed by a zeolitic imidazolate framework (ZIF) through chemical etching and regrowth, followed by quantitative analysis in the core dimension and curvature. We find the nanorod core shows template-effective behavior in its morphological transformation. In the etching event, the nanorod core is spherically carved from its tips. The regrowth on the spherically etched core inside the ZIF gives rise to formation of a raspberry-like branched nanostructure in contrast to the growth of an octahedral shape in bulk condition. We attribute the shell-directed regrowth to void space generated at the interfaces between the etched core and the ZIF shell, intercrystalline gaps in multi-domain ZIF shells, and local structural deformation from the acidic reaction conditions.

KEYWORDS

nanoscale confinement, core-shell structure, gold nanorod, metal-organic framework, oxidative etching, reductive regrowth

1 Introduction

Hybrid nanomaterials, composed of a nanoparticle core and a porous inorganic shell, have shown unique properties and new functions in sensing [1–3], catalysis [4–6], and solid-state reaction [7–9] that cannot be achieved by their single component. The incorporation of the porous shell can allow stability of the nanoparticle core, which is otherwise often sensitive and vulnerable in the solution phase. Depending on the shell porosity and polarity, such hybrid nanomaterials can be utilized as a molecular selective sensor [10, 11]. Catalytic nanoparticle cores, made of platinum or gold, perform enhanced catalytic activity and product selectivity due to synergy effect from the core-shell ensemble [12–14]. In addition, exclusive solid-state reaction of a nanoparticle at high temperature can even be studied in the confining shell as the inorganic shell provides a separate space against heat-driven nanoparticle agglomeration [7, 8].

Nanoscale confinement effect in the hybrid nanostructures can be of great significance to understand and control their unique properties and functions [9, 14–17]. In respect of molecular level, chemical and physical properties of confining molecules could be changed differently than in bulk and often

allow hybrid materials to achieve unprecedented chemical reactivity [17]. For instance, interfacially confined CO₂ molecules in nanocavity between a silver nanoparticle core and a metal-organic framework (MOF) at an ambient condition could undergo a quasi-condensed phase that is only obtained under high pressure [18]. Beyond the molecular regime, unconventional metal nanoparticle growth and morphological transformation could be discovered by the nanoscale confinement in the core-shell nanostructure [9], to which porous inorganic shells give more weight. Yolk-shell nanoreactors were shown to allow precise size control of nanocrystals in confining space [6]. A few nanometer-sized branches on different shapes of gold nanoparticle cores could be grown by mesopores of silica shells [19]. In contrast to commonly used inorganic shells such as silica and zeolite [19–21], however, MOFs have not been applied to investigate the nanoscale confinement effect on morphological changes of metal nanoparticle cores in spite of their great tunability in the physical and chemical properties of nanoscale confining space [22]. Thus, further exploration of the nanoscale confinement effect by MOFs in the hybrid nanostructures would expand the chemistry of metal nanoparticle shape transformation to obtain their optimal properties and functions

Address correspondence to chris@gnu.ac.kr

to desired applications. Also, such examination of nanoscale phenomena would contribute to better understanding of chemical transformation of crystal growth and even biological processes with proteins in the nanometer regime.

Herein we introduced a model system, a gold nanorod encapsulated by a zeolitic imidazolate framework-8 (ZIF-8) in order to investigate nanoscale confinement effect on morphological transformation of the core through chemical etching and regrowth. The ZIF shell has a distinct nanoscale environment with 3.4 Å in pore opening and $\sim 2.5 \text{ nm}^3$ in pore volume [23, 24], which permits size-selective molecular diffusion. The gold nanorod can be a good prototype as a reaction progress indicator in that its shape transformation is easily deduced spectroscopically [25, 26]. An aqueous environment compatible with hexadecyltrimethylammonium bromide (CTAB) stabilized gold nanorods can also be suited to the ZIF shell formation. We found that such nanoscale-confined chemical reaction with the nanorod core was template-effective, displaying slow reactivity in core etching and shell-directed core regrowth.

2 Results and discussion

The overall reaction process with the gold nanorod core encapsulated in a microporous medium, ZIF, is shown in Fig. 1(a). Gold nanorods ($52.9 \pm 4.2 \text{ nm}$ in length and $14.2 \pm 1.1 \text{ nm}$ in width) were first prepared via a seeded growth method (Fig. S1 in the Electronic Supplementary Material (ESM)). The nanorods were encapsulated with ZIF (shell thickness = $150.2 \pm 10.8 \text{ nm}$ in length and $126.3 \pm 14.0 \text{ nm}$ in width) by reacting an aqueous solution of gold nanorods with 2-methylimidazole and zinc nitrate at room temperature (Fig. 1(b) and Fig. S2 in the ESM). As the nanorod solution was injected to the mixture of the ZIF precursors, nucleation and growth of ZIF were initiated on the nanorod surface with CTAB bilayers. Consequently, the core-shell hybrid (Rod@ZIF) was formed as the encapsulated nanorod was centered inside multi-domain ZIF shells. The ZIF shell morphology became shape-anisotropic, adopting the anisotropic core morphology (Fig. S3 in the ESM).

Oxidative etching of the nanorod core in Rod@ZIF was implemented by chloroauric acid and CTAB in methyl alcohol. The nanorod core could be etched spherically while the ZIF shell maintained its original morphology with slight increase in the shell thickness (Fig. 1(c) and Fig. S4 in the ESM). We assume that the increase in relative change of the shell thickness from Rod@ZIF to Sphere@ZIF could be caused by positional reorganization of the ZIF shell domains after local structural deformation. The etching event produced void space at the interfaces between the nanorod core and the adjacent shell, which could spare confined space for further chemical reaction.

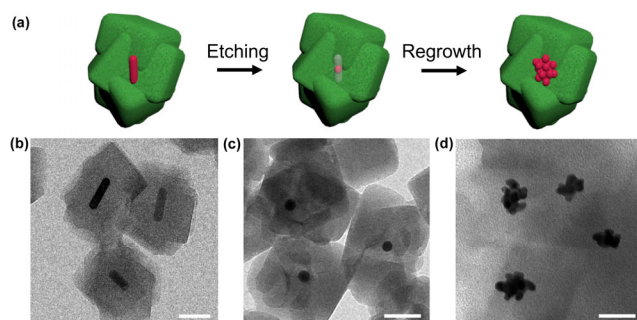


Figure 1 Morphological transformation of the gold nanorod core encapsulated by ZIF. (a) Schematics of Rod@ZIF, Sphere@ZIF, and Sphere@ZIF after reductive regrowth. Transmission electron microscopy (TEM) images of (b) Rod@ZIF, (c) Sphere@ZIF, and (d) Sphere@ZIF after reductive regrowth at 1 min of reaction. Scale bar: 50 nm.

Subsequently, reductive regrowth of the spherically etched core in ZIF was conducted in the presence of chloroauric acid and ascorbic acid. Unlike reductive regrowth in bulk [26], we could grow raspberry-like branched gold nanostructures inside ZIF (Fig. 1(d)).

The degree of oxidative etching on the nanorod core in Rod@ZIF could be controlled by changing chloroauric acid concentration from 66 to 291 μM (Fig. 2(a)). Conproportionation between Au^+ and Au^{3+} led to dissolution of gold atoms on the nanorod tip where atoms were rather under-coordinated [25]. The etching event was monitored via ultraviolet (UV)-visible absorption spectroscopy (Fig. 2(b)). Note that upon the ZIF shell formation, the longitudinal localized surface plasmon resonance (LSPR) band of the nanorod became red-shifted from 781 to 806 nm compared to that without the ZIF shell (Fig. S1(b) in the ESM). The transverse LSPR band at 513 nm showed minute change after the ZIF shell formation. The red shift in the longitudinal LSPR band is attributed to change in the refractive index surrounding the nanorod due to the ZIF shell [27]. The LSPR band shape did not change after the shell formation, reflecting the core nanoparticles were well dispersed and encapsulated without any particle-to-particle aggregation. As the chloroauric acid concentration increased in the etching process, the longitudinal LSPR band started blue-shifted from 806 to 524 nm (see the trace in the inset graph, Fig. 2(b)) and it became barely seen when 291 μM of chloroauric acid was added. The blue shift in the longitudinal LSPR band of Rod@ZIF indicates geometrical transformation of the nanorod core from being anisotropic to isotropic [25, 26].

Quantitative analysis of the core geometry in Rod@ZIF through the etching was accomplished based on TEM images (Figs. 2(c) and 2(d)). First, we confirmed that the nanorod core was intact during the ZIF shell formation and Rod@ZIF particles mostly lay longitudinally on the TEM grid (Fig. S5 in the ESM). Note that we optimized the particle concentration and maintained the rate of drying ($< 5 \text{ min}$) to have the particles deposited horizontally on the TEM grid (Fig. S6 in the ESM). Slight changes in the nanorod length (4.2% from 52.9 ± 4.2 to $50.7 \pm 4.6 \text{ nm}$) and width (2.1% from 14.2 ± 1.1 to $13.9 \pm 1.3 \text{ nm}$) were recognized. It could be attributed to the nanorod position being tilted in the vertical axis due to rugged multi-domain ZIF shells, and its length is seemingly shortened (Fig. S7 in the ESM). The minute decrease in the width could be regarded as within the error range. There was little variation in the nanorod length and width from batch to batch, but the difference was found to increase as the aspect ratio of the nanorod core decreased (Fig. S8 in the ESM). As the etching progressed, the length of the nanorod core in the longitudinal direction decreased linearly from 50.7 nm in Rod@ZIF to 32.7 nm in Semi@ZIF, and 18.0 nm in Sphere@ZIF (Fig. 2(c)). The nanorod width, however, did not change significantly (13.9 nm in Rod@ZIF, 14.6 nm in Semi@ZIF, and 13.0 nm in Sphere@ZIF). Both length and width of the nanorod core were eventually converged to $\sim 13 \text{ nm}$ in Sphere@ZIF. Under higher concentration of chloroauric acid (291 μM), the nanorod core became all etched out, leaving clear void space inside the ZIF shell. While the core etching occurred, the ZIF shell appeared intact with slight rounding of its morphology. Elemental mapping of the series of etched hybrids showed distinguished spatial distribution of Au from the core and Zn from the shell (Fig. 2(d)). The signal for Au diminished as the nanorod core was etched more, matching our geometrical analysis.

In addition to the dimensional analysis, we conducted quantitative analysis of the core morphology over the etching process (Figs. 2(e) and 2(f)). The curvature outlining the

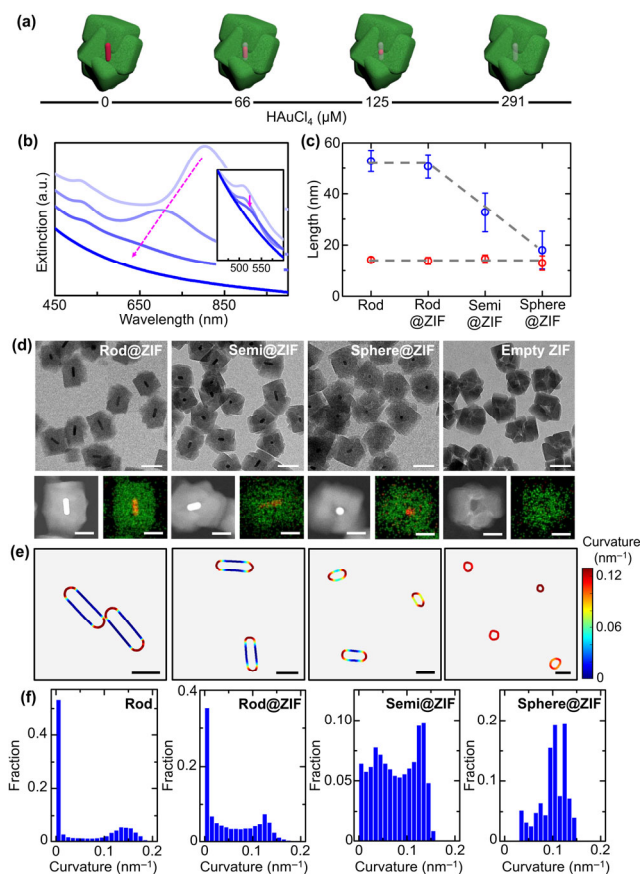


Figure 2 (a) Schematics of Rod@ZIF, Semi@ZIF, Sphere@ZIF, and Empty ZIF after oxidative etching with different HAuCl_4 concentrations (from left to right: 0, 66, 125, and 291 μM , respectively). (b) UV-visible spectra of Rod@ZIF, Semi@ZIF, Sphere@ZIF, and Empty ZIF (from top to bottom: 0, 66, 125, and 291 μM for HAuCl_4 concentration, respectively). The inset graph emphasizes difference between stacked UV-visible spectra from each condition in the range of wavelength from 450 to 600 nm. (c) Dimensional analysis of the core nanorod in each condition. The average width is shown as red and the average length is shown as blue. (d) TEM images of Rod@ZIF, Semi@ZIF, Sphere@ZIF, and Empty ZIF. Elemental mapping (red for Au and green for Zn) with the corresponding TEM image is shown at the bottom, respectively. (e) Representative overlaid surface contours color-coded according to local surface curvature values of the cores from TEM images of the gold nanorod, Rod@ZIF, Semi@ZIF, and Sphere@ZIF (from left to right). (f) Local surface curvature distributions of the gold nanorod, Rod@ZIF, Semi@ZIF, and Sphere@ZIF. The statistics in each condition was obtained from 50 particles. The dotted magenta line in (b) and the dotted gray line in (c) are a guide to the eye. Scale bar: 100 nm in (d) TEM, 50 nm in (d) TEM energy-dispersive X-ray spectroscopy (EDS), and 30 nm in (e).

individual nanorod core was extracted by using image analysis packages, ImageJ and Matlab (see details in Fig. S9 in the ESM). The curvature distribution in each core shape displayed gradual shift in population from $\sim 0 \text{ nm}^{-1}$ for Rod@ZIF to $\sim 0.15 \text{ nm}^{-1}$ for Sphere@ZIF (Fig. 2(f)), indicating the core possesses more curved morphology than that in unetched one. The decrease in the fraction of low curvature values corroborates the preferential longitudinal etching event observed in the aforementioned dimensional analysis. The curvature value also became converged at $\sim 0.15 \text{ nm}^{-1}$ in Sphere@ZIF, indicating its shape-isotropy.

The oxidative etching of the gold nanorod core in Rod@ZIF is considered to follow an etching mechanism with unshelled gold nanorods under the low-driving-force regime. According to Ref. [28], the nanorod etching in the low-driving-force regime occurs when etchants are low in concentration. Its shape

transformation takes place preferentially on the nanorod tip in which gold atoms are less coordinated and more susceptible to the disproportionation reaction between ionic gold species. On the other hand, the high-driving-force regime etching features simultaneous reduction in the nanorod length and width. We found that the etching in Rod@ZIF was terminated more slowly ($\sim 30 \text{ min}$) than that of unshelled nanorods ($\sim 5 \text{ min}$) under the same reaction condition (Movie ESM1). Furthermore, the etching without the ZIF shell appeared to oxidize all gold atoms in the nanorod based on UV-visible spectroscopy and dynamic light scattering (DLS) (Fig. S10 in the ESM), not resulting in spherical particles that were left in Rod@ZIF. We supposed that the originally fast etching kinetics could be suppressed by rather rigid interfacial adhesion between the nanorod side with $\{100\}$ and $\{110\}$ crystal facets and the ZIF shell [29]. Thus, the preferential etching direction on the nanorod tip could still be retained in Rod@ZIF.

The internal structure of Rod@ZIF and core-etched species was investigated using powder X-ray diffraction (XRD) and Brunauer–Emmett–Teller (BET) surface area analysis (Fig. 3). The XRD pattern of Rod@ZIF (Fig. 3(a)) was identical to that of ZIF-8 particles with the corresponding peaks (e.g., 7.3° for $\{011\}$, 10.4° for $\{002\}$, and 12.7° for $\{112\}$) [30], presenting that the ZIF shell in Rod@ZIF maintained its original crystallinity. The gold nanorod core in Rod@ZIF was identified with two high-intensity peaks at 38° for Au $\{111\}$ and 44.5° for Au $\{200\}$ [31]. The core-etched species (Semi@ZIF, Sphere@ZIF, and Empty ZIF) also retained the same signals for ZIF-8 with unaltered relative intensities as Rod@ZIF, indicating subsequent etching on the core particle in Rod@ZIF did not affect the overall crystal structure of the ZIF shell. The XRD peaks assigned to the nanorod core are shown to gradually decrease as the etching occurred further because of the reduced amount of gold in Rod@ZIF. On the other hand, the mean size of the ZIF shell, estimated by the Scherrer equation with full width at half maximum of the first XRD peak [32], was found as 540 \AA for Rod@ZIF and 509 \AA for Sphere@ZIF. We presume that the slight decrease in the mean size could be caused by local degradation of the ZIF shell in the vicinity of intercrystalline ZIF domains, which could be induced by an acidic environment during the etching reaction with chloroauric acid (Table S1 in the ESM). In addition, the microporous properties of Rod@ZIF and Sphere@ZIF were examined by the amount of N_2 adsorbed and desorbed (Fig. 3(b) and Table S2 in the ESM). The BET surface area of Rod@ZIF was recorded as $1,217 \text{ m}^2\cdot\text{g}^{-1}$, which is smaller than that of ZIF-8 ($1,892 \text{ m}^2\cdot\text{g}^{-1}$). The decrease could be attributed to the increased mass added from the nanorod core and potential local non-microporosity originating from multi-domain ZIF intersections. We observed that the BET surface area did not change much between Rod@ZIF and Sphere@ZIF (Table S2 in the ESM), and both isotherm linear plots for N_2 adsorption and desorption were shown to be almost identical (Fig. 3(b)). Although Sphere@ZIF did not contain as many gold atoms as Rod@ZIF and thus we would anticipate

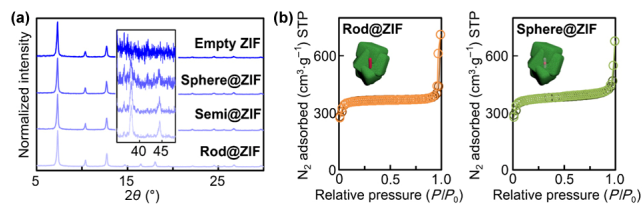


Figure 3 (a) XRD patterns of Rod@ZIF, Semi@ZIF, Sphere@ZIF, and Empty ZIF (from bottom to top). The inset shows magnified XRD signals from 35° to 48° in 2θ . (b) Isotherm linear plots for N_2 adsorption and desorption with Rod@ZIF (left plot) and Sphere@ZIF (right plot).

its higher BET surface area than that of Rod@ZIF, it appears that the etching may result in local structural deformation of the ZIF shells and similar BET surface area in Sphere@ZIF. This speculation could also be supported by an increase in *t*-plot external surface area with respect to BET surface area for Sphere@ZIF (8.8% for ZIF-8, 11.5% for Rod@ZIF, and 14.7% for Sphere@ZIF, Table S2 in the ESM), implying the ZIF shells broken into smaller domains [33].

In comparison with our demonstration on the template-suppressed etching of the nanorod core in nanoscale confinement, we performed reductive regrowth on Sphere@ZIF as a seed in order to study chemical transformation of the core confined in the ZIF shell (Fig. 4). As chloroauric acid and ascorbic acid reacted with Sphere@ZIF, its UV-visible spectrum started to show an LSPR band at 536 nm within 4 min of reaction (Fig. 4(b)). The LSPR band continued to grow by 13 min of reaction and decreased afterwards, the shape of which being broadened and extended to near-infrared wavelengths. After 15 min of reaction, the regrown core nanoparticles seemed to undergo aggregation, which was supported by the solution color changing from pink to light purple (Fig. 4(b) and Fig. S11 in the ESM).

The TEM images over the reaction time display morphological transformation of the spherical core in Sphere@ZIF (Fig. 4(c) and Fig. S12 in the ESM). The reductive growth on the core nanoparticle confined in the ZIF shell was shown as template-directed. Aliquots of the reacting solution at 1, 4, and 12 min of reaction were collected and dried immediately on a TEM grid to avoid any further reaction. Note that there were remaining chemical species deposited on the TEM grid and the corresponding TEM images included blurred areas, and it was difficult to quench the reaction because the reductive regrowth proceeded rapidly (Fig. S13 in the ESM). Otherwise, we would be capable of utilizing the regrown nanostructures for practical applications favorable to the nanobranched structure such as surface-enhanced Raman signaling and photothermal therapy [34, 35].

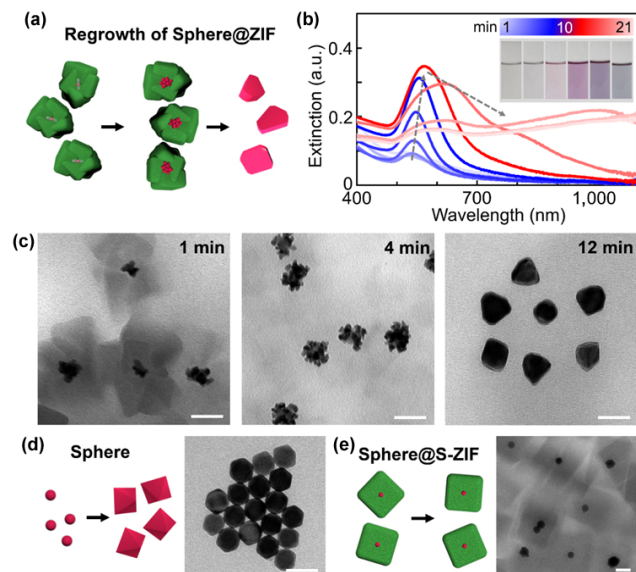


Figure 4 (a) Schematics of the reductive regrowth on Sphere@ZIF over reaction. (b) UV-visible spectra of Sphere@ZIF over the reductive regrowth from 1 to 21 min of reaction (from bluish curves to reddish curves). The inset shows photographs of the solution over the reaction. (c) TEM images of Sphere@ZIF after the reductive regrowth at 1, 4, and 12 min of reaction. (d) Schematics and a TEM image of gold nanospheres after the reductive regrowth at 4 min of reaction. (e) Schematics and a TEM image of Sphere@S-ZIF after the reductive regrowth at 4 min of reaction. The dotted gray lines in (b) are a guide to the eye. Scale bar: 50 nm.

The core nanoparticles obtained at 1 min of reaction (core diameter = 16.5 ± 3.0 nm) were grown larger than the initial core, and raspberry-like branches (branch width = 7.7 ± 2.1 nm) were formed outlining the core nanoparticle (Fig. S12 in the ESM). After 4 min, the core nanoparticles were decorated with distinct branches than those obtained at 1 min of reaction. As the core nanoparticle became larger and more branched, the multi-domain ZIF shells seemed to crack and degrade. The void space where the nanorod core was etched out was calculated as $6,474 \text{ nm}^3$ (85% of the nanorod core volume, Fig. S12(e) in the ESM), which was seemingly enough for the nanobranch formation. However, the nanobranches were shown to grow in all three-dimensional directions toward the void space as well as the adjacent ZIF shell. The complex chemical interactions in the presence of ascorbic acid, chloroauric acid, and hexadecylpyridinium chloride monohydrate (CPC) may cause further structural deformation of the ZIF shell than the etching while the regrowth proceeded. The sample obtained at 12 min of reaction was found to contain only polygonal gold nanoparticles with no ZIF shells. A control experiment with unshelled gold nanospheres was conducted, and we did not observe any raspberry-like branched particles but octahedra (Fig. 4(d) and Fig. S14 in the ESM). Thus, it is assumed that the ZIF shell played an important role in steering the formation of the branched nanostructures.

We suppose that the raspberry-like core regrowth in Sphere@ZIF could be derived from three convoluted factors such as void space generated from the etching, multi-domain properties of the ZIF shell, and local structural deformation of the ZIF shell during the etching and regrowth reactions. To support our hypotheses, we obtained a gold nanosphere encapsulated by a single-domain ZIF shell (Sphere@S-ZIF) and performed the reductive regrowth (Fig. 4(e) and Fig. S15 in the ESM). The ZIF shell in Sphere@S-ZIF was cube-shaped, and one or two spherical cores resided inside the ZIF shell. Through the reductive regrowth in Sphere@S-ZIF, we found no morphological transformation on the core nanoparticle in contrast to our observation with Sphere@ZIF. Note there were some core nanoparticles that underwent transformation at 10 min of reaction (Fig. S15(c) in the ESM), where their ZIF shells were shown to be more decomposed over the extended reaction time. Since the solution was acidic due to chloroauric acid, the ZIF shells even in single-domain Sphere@S-ZIF were naturally degraded and their core nanoparticles became susceptible to the reductive environment. One reasoning for the branched core formation could come from the void space present in Sphere@ZIF (Fig. S12(e) in the ESM). The nanoscale void between the core and the adjacent ZIF shell, generated from etching of the nanorod core, may function as a reservoir for chemical species and facilitate the branch formation on the core. It has been reported that an increase in Au^{3+} and ascorbic acid concentrations results in the formation of gold nanobranches [36]. A recent report demonstrated that nanoscale cavities could help concentrate chemical species inside a porous template [37]. In addition, the multi-domain nature in Sphere@ZIF could be reasoned for the raspberry-like core regrowth. The multi-domain shell may contain hidden mesopores at the intercrystalline ZIF domains. The mesopores were likely to help better transport of chemical species onto the core nanoparticles [38] and it could also serve as nanoscale passages through which gold atoms grew. Moreover, the multiple domains in Sphere@ZIF were assumed to consist of heterogeneous facets than just a single {100} crystal facet which is dominant in cubic ZIF particles (Sphere@S-ZIF). The {100} crystal facet is known to be more resistive and stable in an acidic condition than other

crystal facets [39]. Thus, we presume local structural deformation in the ZIF shell may have occurred over the etching and regrowth reactions in the acidic environment with chloroauric acid, which could also contribute to the branched overgrowth on the core nanoparticle.

The intercrystalline mesoporosity and potential local deformation in the multi-domain shell could be supported examining the TEM images of Rod@ZIF and Sphere@ZIF after multiple washing treatments (Fig. S16 in the ESM). As the hybrid nanoparticles were washed with methyl alcohol, multi-domain ZIF shells were predicted to be vulnerable to domain segregation and the interfacial spaces between the ZIF domains could be enlarged. As the washing was implemented more, the domain segregation in Sphere@ZIF became severe, implying more structural deformation inside. Our assumption on the intersectional conduit-assisted regrowth would further be supported by the reductive regrowth over Rod@ZIF (Fig. S17 in the ESM). The branched nanostructures were grown at the rod tips, which were not observed with unshelled nanorods.

3 Conclusions

In summary, we demonstrated mechanistic insight into tuning the core nanoparticle morphology enclosed by ZIF-8 under the nanoscale confinement. The gold nanorod encapsulated by the ZIF shell underwent template-effective morphological transformation in the etching and regrowth reactions. Under oxidative etching, the nanorod core followed the slow etching process where its tip areas were preferentially etched, while the nanorod core was almost intact in the transversal direction. The regrowth on the spherically etched core produced raspberry-like particles in the ZIF shell. We confirmed that it could be derived from void space between the core and the shell generated from the etching reaction, multi-domain properties of the ZIF shell and consequently existing intercrystalline spacings, and local structural deformation driven by chloroauric acid in both reaction conditions. Our mechanistic understanding on the nanoscale reaction in confined environment would help fine control on developing hybrid nanomaterial with new functions and properties. Further studies on growing different core shapes in the confining environment of various MOFs and acquiring such hybrid nanostructures would be desired to find unique hybrid nanostructures.

4 Materials and methods

4.1 Chemicals

Sodium borohydride (99%, NaBH₄, Sigma-Aldrich), gold(III) chloride trihydrate (99.9%, HAuCl₄·3H₂O, Sigma-Aldrich), silver nitrate (99.0%, AgNO₃, Sigma-Aldrich), CTAB (99.9%, C₁₉H₄₂BrN, Sigma-Aldrich), hexadecylpyridinium chloride monohydrate (> 98%, C₂₁H₃₈ClN·H₂O, TCI), L-ascorbic acid (BioXtra, 99%, C₆H₈O₆, Sigma-Aldrich), zinc nitrate hexahydrate (98%, Zn(NO₃)₂·6H₂O, Sigma-Aldrich), 2-methylimidazole (99%, C₄H₆N₂, Sigma-Aldrich), and methyl alcohol (99.5%, Daejung) were purchased and used without further purification. Deionized water (18.2 MΩ·cm at 25 °C) purified by a Merck Millipore Direct Q3 UV Water Purification System was used for all washing and aqueous solution preparation. All glassware was treated with aqua regia (a mixture of HCl and HNO₃ with a volume ratio of 3:1), repeatedly washed with deionized water and dried immediately before use.

4.2 Synthesis of gold nanorods

Gold nanorods were prepared via literature methods [26, 40].

An aqueous solution of 100 mM CTAB (205 mL) was first prepared in a 250 mL Erlenmeyer flask at 30 °C. The 100 mM CTAB solution (5 mL) was transferred to a 20 mL scintillation vial, and it was mixed with an aqueous solution of 10 mM HAuCl₄ (125 μL). Subsequently, an ice-cold aqueous solution of 10 mM NaBH₄ (300 μL) was quickly injected into the mixture and stirred at 1,150 rpm for 1 min at room temperature. The light brown seed solution was aged at 30 °C for 20 min without stirring. Aqueous solutions of 10 mM HAuCl₄ (10 mL), 10 mM AgNO₃ (1.8 mL), 100 mM ascorbic acid (1.14 mL), and the seed solution (240 μL) were added in sequence into 100 mM CTAB (200 mL) while the solution was stirred at 500 rpm at 30 °C. It was left undisturbed for 2 h. Then, the dark brown solution was centrifuged at 8,000 rpm for 15 min twice. Gold nanorods were dispersed and stored in 50 mM CTAB (5 mL). It showed an extinction at 781 nm with ~ 1.0 in intensity after 40-fold dilution.

4.3 Encapsulation of gold nanorods in ZIF-8 (Rod@ZIF)

Encapsulation of gold nanorods in ZIF-8 was conducted according to a modified method from Ref. [41]. First, the prepared nanorod concentration was adjusted to 25 in extinction, and its CTAB concentration was lowered to 1.5 mM. The nanorod solution (2.04 mL) was centrifuged at 8,000 rpm for 15 min, and supernatant was discarded until leaving the solution by 95 μL. Deionized water (3.06 mL) was added to the solution and mixed well. An aqueous solution of 24 mM Zn(NO₃)₂·6H₂O (3 mL) and the prepared nanorod solution (3 mL) were injected in sequence into an aqueous solution of 1.32 M 2-methylimidazole (3 mL) in a 20 mL scintillation vial while stirred at 500 rpm at room temperature, and the stirring continued for 5 min. It was left undisturbed for 3 h. Then, the cloudy solution was centrifuged at 6,000 rpm for 15 min, and supernatant was discarded. The light brown product was dispersed in methyl alcohol (10 mL) by vortexing and sonication for 5 min. It was centrifuged at 5,000 rpm for 15 min, and supernatant was discarded. The product was dispersed and stored in methyl alcohol (15 mL). It showed an extinction at 806 nm with ~ 1.0 in intensity after 5-fold dilution.

4.4 Etching test of Rod@ZIF (Semi@ZIF, Sphere@ZIF, and Empty ZIF)

Rod@ZIF was etched by using HAuCl₄ and CTAB in methyl alcohol. To find an optimal concentration of HAuCl₄, a test reaction was conducted as follows. The Rod@ZIF solution (9.9 mL, extinction = ~ 2.0) was centrifuged at 8,000 rpm for 10 min, and supernatant was discarded thoroughly. The solvent medium was exchanged with 50 mM CTAB in methyl alcohol (9.9 mL). The solvent-exchanged Rod@ZIF solution (1.5 mL) was transferred into a 2 mL tube (total 6 tubes). A methanolic solution of 10 mM HAuCl₄ (10, 13, 16, 19, 22, and 45 μL) was added into each tube and mixed well. The solutions were transferred to a thermomixer and mixed at 300 rpm for 30 min at 40 °C. Then, the UV-visible spectrum of each solution was measured immediately, and the proper volume of HAuCl₄ was confirmed as 19 μL for obtaining spherical cores in ZIF (Sphere@ZIF). Note that the proper concentration of HAuCl₄ to acquire the spherical shape may vary with respect to used nanorod dimension, which can be referred to literature data [26]. A control experiment with unshelled gold nanorods in methyl alcohol was conducted as mentioned in the etching of Rod@ZIF.

4.5 Large-scale etching of Rod@ZIF (Sphere@ZIF)

The Rod@ZIF solution (19.3 mL, extinction = ~ 2.0) was

centrifuged and solvent-exchanged by using the method mentioned above. A methanolic solution of 10 mM HAuCl₄ (245 μ L) was added to the Rod@ZIF solution in a 50 mL Erlenmeyer flask while stirred at 300 rpm at 40 °C, and it was stirred for 30 min. The light pink solution was centrifuged at 8,000 rpm for 10 min, and supernatant was discarded. The product was dispersed well and stored in methyl alcohol (19.3 mL). It showed an extinction at 528 nm with \sim 0.80 in intensity.

4.6 Regrowth of Sphere@ZIF

The Sphere@ZIF solution (1.5 mL, extinction = \sim 0.80) was centrifuged at 8,000 rpm for 10 min, and supernatant was discarded thoroughly. The solvent medium was exchanged with 100 mM CPC in methyl alcohol (0.2 mL). Methanolic solutions of 10 mM HAuCl₄ (100 μ L), 10 mM ascorbic acid (150 μ L), and Sphere@ZIF (200 μ L) were added in sequence into 100 mM CPC solution (5 mL) in a 20 mL scintillation vial while hand-shaken mildly at each chemical addition. Its UV-visible spectrum was measured every two minutes until it turned clear. Simultaneously, an aliquot (10 μ L) was extracted and dried on a TEM grid for TEM imaging.

In order to terminate the regrowth reaction and obtain the product, the solution after regrowth was quenched by the two following methods, respectively: (i) immediate centrifugation and (ii) immediate dilution and centrifugation. For method (i), aliquots of the product solution (1 mL) right after 1 and 4 min of reaction were centrifuged at 8,000 rpm for 5 s, and supernatant was discarded. The product was dispersed in methyl alcohol (1 mL) before TEM sampling. For method (ii), aliquots of the product solution (1 mL) right after 1 and 4 min of reaction were diluted two times, and the rest of the procedure was followed as method (i).

4.7 Control experiment: encapsulation of gold nanospheres in ZIF-8 (Sphere@S-ZIF) and regrowth of Sphere@S-ZIF

Gold nanospheres stored in 100 mM CPC (10 mL, extinction = \sim 0.8) were prepared according to a modified literature method [26, 40]. The surfactant in the nanosphere solution was first exchanged with 1.5 mM CTAB through two-time centrifugations at 10,000 rpm for 20 min, and the solution was concentrated by 10 times. An aqueous solution of 24 mM Zn(NO₃)₂·6H₂O (1 mL) and the prepared nanosphere solution (1 mL) were injected in sequence into an aqueous solution of 1.32 M 2-methylimidazole (1 mL) in a 20 mL scintillation vial while stirred at 500 rpm at room temperature, and the stirring continued for 5 min. It was left undisturbed for 3 h. The rest of the process was the same as Rod@ZIF. For regrowth, the prepared Sphere@S-ZIF (1.5 mL, extinction = \sim 2.8) was used and redispersed in 100 mM CPC (200 μ L). Methanolic solutions of 100 mM CPC (5 mL), 10 mM HAuCl₄ (100 μ L), 10 mM ascorbic acid (150 μ L), and Sphere@S-ZIF (200 μ L) were sequentially mixed in a 20 mL scintillation vial. The reaction was monitored via a UV-visible spectrometer, and TEM sampling was conducted.

4.8 Control experiment: regrowth of Rod@ZIF

The process was performed as mentioned for regrowth of Sphere@ZIF. Rod@ZIF (1.5 mL, extinction = \sim 2.0) was used and redispersed in 100 mM CPC (200 μ L). Methanolic solutions of 100 mM CPC (5 mL), 10 mM HAuCl₄ (100 μ L), 10 mM ascorbic acid (150 μ L), and Rod@ZIF (200 μ L) were sequentially mixed in a 20 mL scintillation vial. The reaction

was monitored via a UV-visible spectrometer, and TEM sampling was conducted.

4.9 Control experiment: regrowth of gold nanorods and nanospheres

Regrowth of gold nanorods and nanospheres were performed in deionized water instead of methyl alcohol due to poor solubility. The nanorod solution (72 μ L, extinction = \sim 41) was diluted with deionized water (1.4 mL) and redispersed in 100 mM CPC (200 μ L). Aqueous solutions of 100 mM CPC (5 mL), 10 mM HAuCl₄ (100 μ L), 10 mM ascorbic acid (150 μ L), and the nanorod solution (200 μ L) were sequentially mixed in a 20 mL scintillation vial. The reaction was monitored via a UV-visible spectrometer, and TEM sampling was conducted. The nanosphere solution (1.5 mL, extinction = \sim 1.0) was concentrated to 200 μ L. Aqueous solutions of 100 mM CPC (5 mL), 10 mM HAuCl₄ (100 μ L), 10 mM ascorbic acid (150 μ L), and the nanosphere solution (200 μ L) were sequentially mixed in a 20 mL scintillation vial. The reaction was monitored via a UV-visible spectrometer, and TEM sampling was conducted.

4.10 Washing treatment of Rod@ZIF and Sphere@ZIF

Rod@ZIF (1.2 mL, extinction = \sim 2.0) and Sphere@ZIF (1.2 mL, extinction = \sim 1.1) were mixed respectively with methyl alcohol (5 mL), and centrifuged at 8,000 rpm for 10 min. Supernatant (5 mL) was removed, and it was redispersed in methyl alcohol. Each solution (10 μ L) was sampled on a TEM grid. This process was repeated up to 6 times.

4.11 Characterization

An FEI Tecnai 12 transmission electron microscope with a LaB₆ emitter at 120 kV and an FEI Tecnai TF30ST transmission electron microscope with a ZrO/W(100) Schottky emitter at 300 kV were used for material characterization. A JEM-ARM200F Cs-corrected scanning transmission electron microscope (JEOL) was used for elemental mapping. Sample solution (10 μ L) was dropped and dried on a TEM grid (Electron Microscopy Sciences, CF400-CU) before TEM imaging. A JSM-7610F field-emission scanning electron microscope (JEOL) was used for analyzing morphology. Sample solution (20 μ L) was dropped and dried on a silicon wafer (0.5 cm \times 0.5 cm) before the imaging.

Spectroscopic measurements were performed as follows. A UV-visible absorption measurement was conducted using a Genesis 10S UV-visible spectrophotometer with a quartz cuvette (path length = 1 cm). A D8 Advanced A25 (BRUKER) was used for measuring XRD. Sample solution (20 μ L) was dropped and dried on a silicon wafer (0.5 cm \times 0.5 cm), which was repeated 5 times in order to place enough particles for the measurement. A Nano ZS (Malvern Instrument Ltd.) was used for measuring DLS of the gold nanorod solution during the etching. The cell holder was maintained at 40 °C.

A Micromeritics ASAP 2020 accelerated surface area and porosimetry analyzer (Micropore & Chemisorption) was used to analyze the BET surface area. Sample solution was centrifuged at 8,000 rpm for 10 min twice, and supernatant was discarded thoroughly. Residue was dried under vacuum overnight and collected. Pretreatment of the powder was conducted under vacuum at 60 °C for 18 h. Then, N₂ adsorption and desorption were measured at 77.5 K.

4.12 Image analysis

TEM images were first processed by ImageJ, an open source software, and curvature analysis was conducted by our

customized Matlab code. An individual particle (gold nanorod, Rod@ZIF, Semi@ZIF, and Sphere@ZIF) was selected and its TEM image was converted to 8 bit. Gaussian blur function with a sigma of 4 pixels was applied to the image. Contrast of such images was maximized through threshold adjustment to clarify the core shape, giving rise to a mask image with white objects and black background. The mask image was processed via our customized Matlab code in order to obtain curvature values of the core particles. The curvature value was defined by osculating circle in the Matlab code. Consequently, curvature distribution and color map were achieved.

Acknowledgements

This work was supported by the Korea Institute of Energy Technology Evaluation and Planning (No. 20192050100060) from the Korea government Ministry of Trade, Industry, and Energy (MOTIE) and the Korea Basic Science Institute (KBSI) National Research Facilities & Equipment Center (NFEC) (No. 2019R1A6C1010042) from the Ministry of Education of Korea. In addition, this work was partially supported by the Nano-Material Technology Development Program (No. 2009-0082580) and Basic Science Research Program (No. 2020R1C1C1007568) through the National Research Foundation of Korea funded by the Ministry of Science, Information & Communication Technology (ICT), and Future Planning.

Electronic Supplementary Material: Supplementary material (TEM images and UV-visible spectra of gold nanorods and Rod@ZIF, scanning electron microscopy (SEM) images of Rod@ZIF, length and width distributions of the core and the shell in Rod@ZIF, dimensional analysis, orientational distribution of the core in Rod@ZIF, TEM images of Rod@ZIF with different particle concentrations, suggested orientation of the core in Rod@ZIF, dimensional variations of the nanorod core in Rod@ZIF with different batches and aspect ratios, image analysis protocol, UV-visible spectra and DLS spectra of gold nanorod solution during etching, photographs of Sphere@ZIF during reductive regrowth, TEM images of Sphere@ZIF after reductive regrowth and dimensional analysis of raspberry-like product, TEM images of Sphere@ZIF after reductive regrowth and immediate quenching, TEM images of gold nanospheres after reductive regrowth, TEM images of Sphere@S-ZIF after reductive regrowth, TEM images of Sphere@ZIF and Rod@ZIF after washing treatments, TEM images of Rod@ZIF and gold nanorods after reductive regrowth, estimated pH of each reaction condition, porous structure analysis, and a movie of gold nanorods and Rod@ZIF during oxidative etching) is available in the online version of this article at <https://doi.org/10.1007/s12274-020-3042-z>.

References

- Liu, X. H.; Zhang, J.; Wang, L. W.; Yang, T. L.; Guo, X. Z.; Wu, S. H.; Wang, S. R. 3D hierarchically porous ZnO structures and their functionalization by Aunanoparticles for gas sensors. *J. Mater. Chem.* **2011**, *21*, 349–356.
- He, L. C.; Liu, Y.; Liu, J. Z.; Xiong, Y. S.; Zheng, J. Z.; Liu, Y. L.; Tang, Z. Y. Core-shell noble-metal@metal-organic-framework nanoparticles with highly selective sensing property. *Angew. Chem., Int. Ed.* **2013**, *52*, 3741–3745.
- Xu, Z. D.; Yang, L. Z.; Xu, C. L. Pt@UiO-66 heterostructures for highly selective detection of hydrogen peroxide with an extended linear range. *Anal. Chem.* **2015**, *87*, 3438–3444.
- Zhang, Q.; Lee, I.; Joo, J. B.; Zaera, F.; Yin, Y. D. Core-shell nanostructured catalysts. *Acc. Chem. Res.* **2013**, *46*, 1816–1824.
- Moon, H. R.; Lim, D. W.; Suh, M. P. Fabrication of metal nanoparticles in metal-organic frameworks. *Chem. Soc. Rev.* **2013**, *42*, 1807–1824.
- Lee, J.; Kim, S. M.; Lee, I. S. Functionalization of hollow nanoparticles for nanoreactor applications. *Nano Today* **2014**, *9*, 631–667.
- Park, J. C.; Bang, J. U.; Lee, J.; Ko, C. H.; Song, H. Ni@SiO₂ yolk-shell nanoreactor catalysts: High temperature stability and recyclability. *J. Mater. Chem.* **2010**, *20*, 1239–1246.
- Koo, J. H.; Lee, S. W.; Park, J. Y.; Lee, I. S. Nanospace-confined high-temperature solid-state reactions: Versatile synthetic route for high-diversity pool of catalytic nanocrystals. *Chem. Mater.* **2017**, *29*, 9463–9471.
- Kumar, A.; Jeon, K. W.; Kumari, N.; Lee, I. S. Spatially confined formation and transformation of nanocrystals within nanometer-sized reaction media. *Acc. Chem. Res.* **2018**, *51*, 2867–2879.
- Sugikawa, K.; Nagata, S.; Furukawa, Y.; Kokado, K.; Sada, K. Stable and functional gold nanorod composites with a metal-organic framework crystalline shell. *Chem. Mater.* **2013**, *25*, 2565–2570.
- Falcaro, P.; Ricco, R.; Yazdi, A.; Imaz, I.; Furukawa, S.; Maspoch, D.; Ameloot, R.; Evans, J. D.; Doonan, C. J. Application of metal and metal oxide nanoparticles@MOFs. *Coord. Chem. Rev.* **2016**, *307*, 237–254.
- Ke, F.; Zhu, J. F.; Qiu, L. G.; Jiang, X. Controlled synthesis of novel Au@MIL-100(Fe) core-shell nanoparticles with enhanced catalytic performance. *Chem. Commun.* **2013**, *49*, 1267–1269.
- Zhou, J. J.; Wang, P.; Wang, C. X.; Goh, Y. T.; Fang, Z.; Messersmith, P. B.; Duan, H. W. Versatile core-shell nanoparticle@metal-organic framework nanohybrids: Exploiting mussel-inspired polydopamine for tailored structural integration. *ACS Nano* **2015**, *9*, 6951–6960.
- Li, G. D.; Zhao, S. L.; Zhang, Y.; Tang, Z. Y. Metal-organic frameworks encapsulating active nanoparticles as emerging composites for catalysis: Recent progress and perspectives. *Adv. Mater.* **2018**, *30*, 1800702.
- Liu, Y. L.; Tang, Z. Y. Multifunctional nanoparticle@MOF core-shell nanostructures. *Adv. Mater.* **2013**, *25*, 5819–5825.
- Chen, J. X.; Feng, J.; Yang, F.; Aleisa, R.; Zhang, Q.; Yin, Y. D. Space-confined seeded growth of Cu nanorods with strong surface plasmon resonance for photothermal actuation. *Angew. Chem., Int. Ed.* **2019**, *131*, 9376–9382.
- Grommet, A. B.; Feller, M.; Klajn, R. Chemical reactivity under nanoconfinement. *Nat. Nanotechnol.* **2020**, *15*, 256–271.
- Lee, H. K.; Lee, Y. H.; Morabito, J. V.; Liu, Y. J.; Koh, C. S. L.; Phang, I. Y.; Pedireddy, S.; Han, X. M.; Chou, L. Y.; Tsung, C. K. et al. Driving CO₂ to a quasi-condensed phase at the interface between a nanoparticle surface and a metal-organic framework at 1 Bar and 298 K. *J. Am. Chem. Soc.* **2017**, *139*, 11513–11518.
- Sanz-Ortiz, M. N.; Sentosun, K.; Bals, S.; Liz-Marzán, L. M. Templated growth of surface enhanced Raman scattering-active branched gold nanoparticles within radial mesoporous silica shells. *ACS Nano* **2015**, *9*, 10489–10497.
- Deng, T. S.; van der Hoeven, J. E. S.; Yalcin, A. O.; Zandbergen, H. W.; van Huis, M. A.; van Blaaderen, A. Oxidative etching and metal overgrowth of gold nanorods within mesoporous silica shells. *Chem. Mater.* **2015**, *27*, 7196–7203.
- Wu, Z. H.; Liang, Y. L.; Guo, Q.; Zhang, K. Q.; Liang, S. F.; Yang, L. Y.; Xiao, Q.; Wang, D. Study on selective oxidations of gold nanorod and mesoporous silica-coated gold nanorod. *J. Mater. Sci.* **2019**, *54*, 8133–8147.
- Furukawa, H.; Cordova, K. E.; O’Keeffe, M.; Yaghi, O. M. The chemistry and applications of metal-organic frameworks. *Science* **2013**, *341*, 1230444.
- Park, K. S.; Ni, Z.; Côté, A. P.; Choi, J. Y.; Huang, R. D.; Uribe-Romo, F. J.; Chae, H. K.; O’Keeffe, M.; Yaghi, O. M. Exceptional chemical and thermal stability of zeolitic imidazolate frameworks. *Proc. Natl. Acad. Sci. USA* **2006**, *103*, 10186–10191.
- Huang, X. C.; Lin, Y. Y.; Zhang, J. P.; Chen, X. M. Ligand-directed strategy for zeolite-type metal-organic frameworks: Zinc(II) imidazolates with unusual zeolitic topologies. *Angew. Chem., Int. Ed.* **2006**, *45*, 1557–1559.
- Rodríguez-Fernández, J.; Pérez-Juste, J.; Mulvaney, P.; Liz-Marzán, L. M. Spatially-directed oxidation of gold nanoparticles by Au(III)-CTAB complexes. *J. Phys. Chem. B* **2005**, *109*, 14257–14261.
- O’Brien, M. N.; Jones, M. R.; Brown, K. A.; Mirkin, C. A. Universal noble metal nanoparticle seeds realized through iterative reductive

- growth and oxidative dissolution reactions. *J. Am. Chem. Soc.* **2014**, *136*, 7603–7606.
- [27] Underwood, S.; Mulvaney, P. Effect of the solution refractive index on the color of gold colloids. *Langmuir* **1994**, *10*, 3427–3430.
- [28] Hauwiler, M. R.; Ondry, J. C.; Chan, C. M.; Khandekar, P.; Yu, J.; Alivisatos, A. P. Gold nanocrystal etching as a means of probing the dynamic chemical environment in graphene liquid cell electron microscopy. *J. Am. Chem. Soc.* **2019**, *141*, 4428–4437.
- [29] Hirakawa, T.; Kamat, P. V. Charge separation and catalytic activity of Ag@TiO₂ core-shell composite clusters under UV-irradiation. *J. Am. Chem. Soc.* **2005**, *127*, 3928–3934.
- [30] Pan, Y. C.; Liu, Y. Y.; Zeng, G. F.; Zhao, L.; Lai, Z. P. Rapid synthesis of zeolitic imidazolate framework-8 (ZIF-8) nanocrystals in an aqueous system. *Chem. Commun.* **2011**, *47*, 2071–2073.
- [31] Ayyappan, S.; Gopalan, R. S.; Subbanna, G. N.; Rao, C. N. R. Nanoparticles of Ag, Au, Pd, and Cu produced by alcohol reduction of the salts. *J. Mater. Res.* **1997**, *12*, 398–401.
- [32] Cullity, B. D.; Stock, S. R. *Elements of X-ray Diffraction*; 3rd ed. Prentice Hall: Upper Saddle River, 2001; pp 96–102.
- [33] Tsai, C. W.; Langner, E. H. G. The effect of synthesis temperature on the particle size of nano-ZIF-8. *Micropor. Mesopor. Mater.* **2016**, *221*, 8–13.
- [34] Vijayaraghavan, P.; Liu, C. H.; Hwang, K. C. Synthesis of multi-branched gold nanoechinus using a gemini cationic surfactant and its application for surface enhanced Raman scattering. *ACS Appl. Mater. Interfaces* **2016**, *8*, 23909–23919.
- [35] Ong, Z. Y.; Chen, S.; Nabavi, E.; Regoutz, A.; Payne, D. J.; Elson, D. S.; Dexter, D. T.; Dunlop, I. E.; Porter, A. E. Multibranching gold nanoparticles with intrinsic LAT-1 targeting capabilities for selective photothermal therapy of breast cancer. *ACS Appl. Mater. Interfaces* **2017**, *9*, 39259–39270.
- [36] Kuo, C. H.; Huang, M. H. Synthesis of branched gold nanocrystals by a seeding growth approach. *Langmuir* **2005**, *21*, 2012–2016.
- [37] Sim, H. Y. F.; Lee, H. K.; Han, X. M.; Koh, C. S. L.; Phan-Quang, G. C.; Lay, C. L.; Kao, Y. C.; Phang, I. Y.; Yeow, E. K. L.; Ling, X. Y. Concentrating immiscible molecules at solid@MOF interfacial nanocavities to drive an inert gas-liquid reaction at ambient conditions. *Angew. Chem., Int. Ed.* **2018**, *57*, 17058–17062.
- [38] Zhou, S.; Wei, Y. Y.; Li, L. B.; Duan, Y. F.; Hou, Q. Q.; Zhang, L. L.; Ding, L. X.; Xue, J.; Wang, H. H.; Caro, J. Paralyzed membrane: Current-driven synthesis of a metal-organic framework with sharpened propene/propane separation. *Sci. Adv.* **2018**, *4*, eaau1393.
- [39] Pang, S. H.; Han, C.; Sholl, D. S.; Jones, C. W.; Lively, R. P. Facet-specific stability of ZIF-8 in the presence of acid gases dissolved in aqueous solutions. *Chem. Mater.* **2016**, *28*, 6960–6967.
- [40] Kim, J.; Song, X. H.; Kim, A.; Luo, B. B.; Smith, J. W.; Ou, Z. H.; Wu, Z. X.; Chen, Q. Reconfigurable polymer shells on shape-anisotropic gold nanoparticle cores. *Macromol. Rapid Commun.* **2018**, *39*, 1800101.
- [41] Zheng, G. C.; de Marchi, S.; López-Puente, V.; Sentosun, K.; Polavarapu, L.; Pérez-Juste, I.; Hill, E. H.; Bals, S.; Liz-Marzán, L. M.; Pastoriza-Santos, I.; Pérez-Juste, J. Encapsulation of single plasmonic nanoparticles within ZIF-8 and SERS analysis of the MOF flexibility. *Small* **2016**, *12*, 3935–3943.